Inorg. Chem. **2009**, *48*, 2181−2192

Controlled Synthesis, Characterization, and Morphology-Dependent Reducibility of Ceria−Zirconia−Yttria Solid Solutions with Nanorod-like, Microspherical, Microbowknot-like, and Micro-octahedral Shapes

Yujuan Zhang, Lei Zhang, Jiguang Deng, Hongxing Dai,* and Hong He

Laboratory of Catalysis Chemistry and Nanoscience, Department of Chemistry and Chemical Engineering, College of Environmental and Energy Engineering, Beijing University of Technology, Beijing 100124, P. R. China

Received November 15, 2008

By adopting the strategy of triblock copolymer (Pluronic P123) or cetyltrimethylammonium bromide (CTAB) assisted hydrothermal treatment, we fabricated cubic fluorite-type $Ce_{0.6}Zr_{0.3}Y_{0.1}O_2$ (CZY) solid solution polycrystallites with various morphologies. These materials were characterized by means of techniques such as X-ray diffraction, scanning electron microscopy, transmission electron microscopy, selected-area electron diffraction, X-ray photoelectron spectroscopy, thermogravimetry, laser Raman, Fourier-transfer infrared spectroscopy, hydrogen temperature-programmed reduction, and surface area measurements. It is found that the nanorod-like, microspherical, microbowknot-like, and micro-octahedral CZY particles were respectively generated hydrothermally with CTAB at 120 °C for 72 h and with P123 at 100, 120, and 240 °C for 48 h after calcination at 550 °C for 3 h. There was a copresence of Ce^{3+} and Ce^{4+} in the CZY samples that led to the formation of oxygen vacancies. We observed a good correlation of low-temperature reducibility with the morphology of the CZY samples. The reducibility of these nano- and micromaterials at low temperatures (240−550 °C) enhanced in the order micro-octahedral CZY < microspherical CZY < microbowknot-like CZY < nanorod-like CZY. The formation mechanism of CZY with various morphologies was discussed.

1. Introduction

It has been generally accepted that morphology-controlled fabrication of inorganic nanomaterials is of scientific and technological significance due to their shape- and size-dependent properties. These unique properties make them highly promising for a wide range of applications in heterogeneous catalysis, opto- and microelectronics, magnetics, and biology.[1] Although many methods (e.g., template-direction, vapor-phase transportation, electrochemical deposition, soluble complex precursor thermolysis, and solvo- and hydrothermal treatment) have been proposed for the morphosynthesis of nanoparticles with unique architecture,[1b−i,2] hydrothermal strategy has been proven to be an effective and economical approach due to its several advantages: (i) a single-step low-temperature process, (ii) facile control in composition and morphology, and (iii) wide suitability for metal precursors.

Ceria is one of the most intensively investigated rare earth oxides. Due to the good oxygen storage capacity (OSC) that

* To whom correspondence should be addressed. Phone: +86-10-67396588. Fax: +86-10-67396588. E-mail: hxdai@bjut.edu.cn.

(1) (a) Narayanan, R.; El-Sayed, M. A. *J. Phys. Chem. B* **2005**, *109*, 12663. (b) Ahmadi, T. S.; Wang, Z. L.; Green, T. C.; Henglein, A.; El-Sayed, M. A. *Science* **1996**, *272*, 1924. (c) Lisiecki, I. *J. Phys. Chem. B* **2005**, *109*, 12231. (d) Hu, J. T.; Odom, T. W.; Lieber, C. M. *Acc. Chem. Res.* **1999**, *32*, 435. (e) Xia, Y. N.; Yang, P. D.; Sun, Y. G.; Wu, Y. Y.; Mayers, B.; Gates, B.; Yin, Y. D.; Kim, F.; Yan, H. Q. *Adv. Mater.* **2003**, *15*, 353. (f) Wu, Y. Y.; Yan, H. Q.; Huang, M.; Messer, B.; Song, J. H.; Yang, P. D. *Chem.−Eur. J.* **2002**, *8*, 1260. (g) Alivisatos, A. P. *Science* **1996**, *271*, 933. (h) Partzke, G. R.; Krumeich, F.; Nesper, R. *Angew. Chem., Int. Ed.* **2002**, *41*, 2446. (i) Sun, S.; Murray, C. B.; Weller, D.; Folks, L.; Moser, A. *Science* **2000**, *287*, 1989. (j) Bruchez, M.; Moronne, M.; Gin, P.; Weiss, S.; Alivisatos, A. P. *Science* **1998**, *281*, 2013.

(2) (a) Huang, M. H.; Wu, Y. Y.; Feick, H.; Tran, N.; Weber, E.; Yang, P. D. *Adv. Mater.* **2001**, *13*, 113. (b) Vantomme, A.; Yuan, Z. Y.; Du, G. H.; Su, B. L. *Langmuir* **2005**, *21*, 1132. (c) Xu, L. F.; Guo, Y.; Liao, Q.; Zhang, J. P.; Xu, D. S. *J. Phys. Chem. B* **2005**, *109*, 13519. (d) Peng, Z. A.; Peng, X. G. *J. Am. Chem. Soc.* **2001**, *123*, 1389. (e) Chen, M.; Xie, Y.; Lu, J.; Xiong, Y. J.; Zhang, S. Y.; Qian, Y. T.; Liu, X. M. *J. Mater Chem.* **2002**, *12*, 748. (f) Zhang, J.; Sun, L. D.; Yin, J. L.; Su, H. L.; Liao, C. S.; Yan, C. H. *Chem. Mater.* **2002**, *14*, 4172. (g) Zhang, Y. W.; Yan, Z. G.; You, L. P.; Si, R.; Yan, C. H. *Eur. J. Inorg. Chem.* **2003**, *22*, 4099. (h) Wang, X.; Li, Y. D. *Angew. Chem., Int. Ed.* **2002**, *41*, 4790.

10.1021/ic802195j CCC: $40.75
Published on Web 02/04/2009

is associated with the rich oxygen vacancies and low redox potential between Ce^{3+} and Ce^{4+},[3] CeO_2 has been used as a promoter of three-way catalysts for the removal of automotive exhaust. The doping of zirconium to the CeO_2 lattice can significantly enhance the OSC, redox ability, thermal stability, and surface area. In the past years, a number of works on the synthesis, characterization, and catalytic properties of $Ce_{1-x}Zr_xO_2$solid solutions have been done. Recent studies on the CeO_2-based materials have focused on the development of synthetic approaches toward size- and shape-controlled nanostructures (e.g., nanodots,[4] nanorods,[2b,5] nanowires,[6] and nanotubes[7]) and the characterization of their size- and shape-dependent properties.[4,5b,6f] For example, some groups fabricated size-tunable CeO_2 nanocrystals via various wet chemical approaches (including modified precipitation, alcohothermal treatment, microemulsion, and the sonochemical method) and investigated their size-dependent ultraviolet light absorption behaviors in order to clarify the confinement effects in CeO_2.[4] By adopting a hydrothermal route, Li et al. synthesized single-crystalline CeO_2 nanorods that showed enhanced CO conversion activity.[5b] Via a solution-phase pathway with sodium bis(2-ethylhexyl) sulfosuccinate as a structure-directing agent, Chen et al. generated polycrystalline CeO_2 nanowires that exhibited a size-dependent effect on Raman spectra.[6f]

However, reports on the selective fabrication of nano- and microsized CeO_2 and $Ce_{1-x}Zr_xO_2$ solid solutions with different morphologies are scarcely found in the literature. The investigation of shape-dependent properties (e.g., the OSC, reducibility, and catalytic activity) has remained a challenge. For the nanostructured CeO_2 materials, both surface and bulk oxygen atoms could be utilized in the redox process, whereas for their bulk powders, only the surface oxygen atoms were useful.[3c] It is known that the relationship between the OSC and surface structure related to a specific crystalline shape for nanometer CeO_2 or $Ce_{1-x}Zr_xO_2$ is still a subject of vivid investigation and debate.[3a,c,5b,8] In order to clarify such a relationship, it is highly desired to selectively make ceria−zirconia-based nano- and micromaterials of different shapes and investigate their size- and morphology-dependent physicochemical properties.

In recent years, metal-doped ceria−zirconia solid solutions have been investigated. The partial substitution of Ce in CeO_2 by other cations, M (M = Zr, Pr, Gd), could promote the formation of oxygen vacancies, which can hasten the diffusion rate of oxygen and enhance combustion activity.[9] The doping of trivalent rare earth cations (e.g., La^{3+}, Y^{3+}, or Pr^{3+}) into the $Ce_{1-x}Zr_xO_2$ lattice could noticeably improve thermal stability, redox ability, and OSC values of the solid solutions.[10] Yttria is a good dopant for CeO_2, ZrO_2, or $Ce_{1-x}Zr_xO_2$. In past years, yttria-doped ceria (e.g., $(YO_{1.5})_{0.2}(CeO_2)_{0.8}$[11]), yttria-doped zirconia (e.g., $(YO_{1.5})_{0.15}(ZrO_2)_{0.85}$[11]), and yttria-doped ceria−zirconia solid solutions (e.g., $(CeO_2)_{0.8x}(ZrO_2)_{0.8-0.8x}(YO_{1.5})_{0.2}$ ($x = 0-1$)[12] and $(CeO_2)_{0.1}(ZrO_2)_{0.88}(YO_{1.5})_{0.02}$[13]) have been investigated intensively and extensively. These materials exhibit an enhanced high conductivity and transference number of the oxide ion due to the creation of oxygen vacancies. In our group, we reported that, with the inclusion of a small amount of Y^{3+} in the $RE_{0.6}Zr_{0.4}O_2$ (RE = Ce, Pr) lattice, the as-obtained $RE_{0.6}Zr_{0.35}Y_{0.05}O_2$ solid solution exhibited enriched oxygen vacancies, enhanced lattice oxygen mobility, and better oxygen storage and release (redox) ability.[14] The possibility of controlling the physicochemical properties of a material by tailoring its crystalline structure and morphology is a current topic of great interest. A lot of work on the control of the morphology and properties of materials reveals that there is a presence of good correlation between particle morphology and physicochemical properties.[15] Such a morphology-dependent behavior inspires scientific researchers to explore strategies for the fabrication of specifically morphological nano- and micromaterials.

By introducing a surfactant of cetyltrimethylammonium bromide (CTAB) or triblock copolymer poly(ethylene glycol)-*block*-poly(propylene glycol)-*block*-poly(ethylene glycol) ($EO_{20}PO_{70}EO_{20}$, P123, $M_{av.}$ = 5800, Aldrich) to a mixed

(3) (a) Trovarelli, A. *Catalysis by Ceria and Related Materials*, 2nd ed.; Dunod: London, 2002. (b) Powell, B. R.; Bloink, R. L.; Eickel, C. C. *J. Am. Ceram. Soc.* **1988**, *71*, 104. (c) Kašpar, J.; Fornasiero, P.; Graziani, M. *Catal. Today* **1999**, *50*, 285. (d) Si, R.; Zhang, Y. W.; Li, S. J.; Lin, B. X.; Yan, C. H. *J. Phys. Chem. B* **2004**, *108*, 12481.

(4) (a) Masui, T.; Fujiwara, K.; Machida, K. I.; Adachi, G. Y. *Chem. Mater.* **1997**, *9*, 2197. (b) Zhang, Y. W.; Si, R.; Liao, C. S.; Yan, C. H.; Xiao, C. X.; Kou, Y. *J. Phys. Chem. B* **2003**, *107*, 10159. (c) Si, R.; Zhang, Y. W.; You, L. P.; Yan, C. H. *Angew. Chem., Int. Ed.* **2005**, *44*, 3256. (d) Inoue, M.; Kimura, M.; Inui, T. *Chem. Commun.* **1999**, 957. (e) Yin, L. X.; Wang, Y. Q.; Pang, G. S.; Koltypin, Y.; Gedanken, A. *J. Colloid Interface Sci.* **2002**, *246*, 78. (f) Wang, H.; Zhu, J. J.; Zhu, J. M.; Liao, X. H.; Xu, S.; Ding, T.; Chen, H. Y. *Phys. Chem. Chem. Phys.* **2002**, *4*, 3794. (g) Zhang, F.; Chan, S.-W.; Spanier, J. E.; Apak, E.; Jin, Q.; Robinson, R. D.; Herman, I. P. *Appl. Phys. Lett.* **2002**, *80*, 127. (h) Zhang, F.; Jin, Q.; Chan, S.-W. *J. Appl. Phys.* **2004**, *95*, 4319. (i) Tsunekawa, S.; Fukuda, T. *J. Appl. Phys.* **2000**, *87*, 1318.

(5) (a) Kuiry, S. C.; Patil, S. D.; Deshpande, S.; Seal, S. *J. Phys. Chem. B* **2005**, *109*, 6936. (b) Zhou, K. B.; Wang, X.; Sun, X. M.; Peng, Q.; Li, Y. D. *J. Catal.* **2005**, *229*, 206.

(6) (a) Tang, B.; Zhuo, L. H.; Ge, J. C.; Wang, G. L.; Shi, Z. Q.; Niu, J. Y. *Chem. Commun.* **2005**, 3565. (b) Wu, G. S.; Xie, T.; Yuan, X. Y.; Cheng, B. C.; Zhang, L. D. *Mater. Res. Bull.* **2004**, *39*, 1023. (c) Yada, M.; Sakai, S.; Torikai, T.; Watari, T.; Furuta, S.; Katsuki, H. *Adv. Mater.* **2004**, *16*, 1222. (d) Yang, R.; Guo, L. *J. Mater. Sci.* **2005**, *40*, 1035. (e) La, R. J.; Hu, Z. A.; Li, H. L.; Shang, X. L.; Yang, Y. Y. *Mater. Sci. Eng., A* **2004**, *368*, 145. (f) Sun, C. W.; Li, H.; Wang, Z. X.; Chen, L. Q.; Huang, X. J. *Chem. Lett.* **2004**, *33*, 662.

(7) (a) Yang, R.; Guo, L. *Chin. J. Inorg. Chem.* **2004**, *20*, 152. (b) Han, W.-Q.; Wu, L.; Zhu, Y. *J. Am. Chem. Soc.* **2005**, *127*, 12814.

(8) (a) Di Monte, R.; Kaspar, J. *Top. Catal.* **2004**, *28*, 47. (b) Madier, Y.; Descorme, C.; Govic, A. M. L.; Duprez, D. *J. Phys. Chem. B* **1999**, *103*, 10999.

(9) Fang, P.; Luo, M.-F.; Lu, J.-Q.; Cen, S.-Q.; Yan, X.-Y.; Wang, X.-X. *Thermochim. Acta* **2008**, *478*, 45.

(10) (a) Si, R.; Zhang, Y.-W.; Wang, L.-M.; Li, S.-J.; Lin, B.-X.; Chu, W.-S.; Wu, Z.-Y.; Yan, C.-H. *J. Phys. Chem. C* **2007**, *111*, 787. (b) Narula, C. K.; Haack, L. P.; Chun, W.; Jen, H.-W.; Graham, G. W. *J. Phys. Chem. B* **1999**, *103*, 3634.

(11) Mitsuyasu, H.; Nonaka, Y.; Eguchi, K.; Arai, H. *J. Solid State Chem.* **1997**, *129*, 74.

(12) Sakai, N.; Yamaji, K.; Xiong, Y. P.; Kishimoto, H.; Horita, T.; Yokokawa, H. *J. Electroceram.* **2004**, *13*, 677.

(13) Chiou, B.-S.; Dai, H.-T.; Duh, J.-G. *J. Am. Ceram. Soc.* **1990**, *73*, 866.

(14) (a) He, H.; Dai, H. X.; Ng, L. H.; Wong, K. W.; Au, C. T. *J. Catal.* **2002**, *206*, 1. (b) He, H.; Dai, H. X.; Wong, K. W.; Au, C. T. *Appl. Catal., A* **2003**, *251*, 61. (c) He, H.; Dai, H. X.; Au, C. T. *Catal. Today* **2004**, *90*, 245.

(15) (a) Ho, C.; Yu, J. C.; Kwong, T.; Mak, A. C.; Lai, S. *Chem. Mater.* **2005**, *17*, 4514. (b) Zhou, L.; Wang, W.; Xu, H.; Sun, S. *Cryst. Growth Des.* **2008**, *8*, 3595. (c) Testino, A.; Bellobono, I. R.; Buscaglia, V.; Canevali, C.; D'Arienzo, M.; Polizzi, S.; Scotti, R.; Morazzoni, F. *J. Am. Chem. Soc.* **2007**, *129*, 3564.

Table 1. Fabrication Conditions and Surface Compositions of the CZY Samples

sample	fabrication conditions (surfactant/hydrothermal temperature (°C)/time (h))	surface Zr/Ce atomic ratio[a]	surface Y/Ce atomic ratio[a]	O_{ads}/O_{latt}[b]	Ce^{3+}/Ce^{4+}[c]
CZY-CTAB-120	CTAB/120/72	0.64 (0.50)[d]	0.15 (0.17)[d]	0.77	0.24
CZY-P123-100	P123/100/48	0.67 (0.50)	0.16 (0.17)	0.39	0.09
CZY-P123-120	P123/120/48	0.67 (0.50)	0.19 (0.17)	0.56	0.19
CZY-P123-240	P123/240/48	0.65 (0.50)	0.15 (0.17)	0.48	0.10

[a] The data were estimated according to the results of XPS investigations. [b] O_{ads}/O_{latt} denotes the atomic ratio of surface adsorbed oxygen (O_{ads}) and lattice oxygen (O_{latt}) species in the sample. [c] Ce^{3+}/Ce^{4+} denotes the atomic ratio of surface Ce^{3+} and Ce^{4+} contents in the sample. [d] The data in parentheses were calculated according to the nominal bulk composition of the sample.

solution containing stoichiometric Ce^{3+}, Zr^{4+}, and Y^{3+} ions and treating the mixture under different hydrothermal conditions, we have successfully generated a series of ceria−zirconia−yttria solid solutions that displayed various morphologies. In this article, we report the facile surfactant-assisted hydrothermal fabrication, characterization, and morphology-dependent reducibility of $Ce_{0.6}Zr_{0.3}Y_{0.1}O_2$ with shapes of nano- and microrods, spheres, bowknots, and octahedra.

2. Experimental Section

2.1. Synthesis. The $Ce_{0.6}Zr_{0.3}Y_{0.1}O_2$ (CZY) samples with morphologies of nano- or microrods, spheres, bowknots, and octahedra were synthesized using the surfactant (P123 or CTAB)-assisted hydrothermal method with $Ce(NO_3)_3 \cdot 6H_2O$, $ZrO(NO_3)_2 \cdot 2H_2O$, and $Y(NO_3)_3 \cdot 6H_2O$ as the metal sources and urea as the precipitation agent. Under magnetic stirring and at room temperature (RT), stoichiometric amounts of $Ce(NO_3)_3 \cdot 6H_2O$ (6.00 mmol), $ZrO(NO_3)_2 \cdot 2H_2O$ (3.00 mmol), and $Y(NO_3)_3 \cdot 6H_2O$ (1.00 mmol) were first dissolved in 5 mL of deionized water; the mixed solution was then added to the surfactant-containing solution (20.0 mmol of CTAB + 75 mL of deionized water or 0.20 mmol of triblock copolymer Pluronic P123 + 25 mL of deionized water). After being well-mixed, 200 mmol of urea was finally added dropwise to the above mixed solution under stirring for 2 h. The CZY/CTAB/urea and CZY/P123/urea molar ratios were 1:2:20 and 1:0.02:20, respectively. The coprecipitation mixture solution was sealed in a glass vessel and placed into an oven for aging treatment at 80 °C for 72 h. The obtained milky slurry was transferred to a 100 mL Telflon-lined stainless steel autoclave (packed volume = 60 mL) for hydrothermal treatment at 100, 120, 160, or 240 °C for 48 or 72 h. After being cooled down to RT, filtered, and washed with deionized water three or four times, the obtained powders were dried at 60 °C overnight and calcined in an air flow of 80 mL min^{-1} at a heating rate of 1 °C min^{-1} from RT to 550 °C and kept at this temperature for 3 h, thus obtaining the yellow product. The samples derived from the CTAB-assisted hydrothermal treatment at 120 and 160 °C for 72 h were denoted as CZY-CTAB-120 and CZY-CTAB-160, whereas those derived from the P123-assisted hydrothermal treatment at 100, 120, and 240 °C for 48 h were denoted as CZY-P123-100, CZY-P123-120, and CZY-P123-240, respectively (see Table 1 for fabrication conditions and surface compositions of the CZY samples). It should be noted that all of the chemicals (A.R. in purity) employed in the present study were purchased from Beijing Chemical Reagent Company (unless otherwise indicated) and used without further purification.

2.2. Characterization. X-ray diffraction (XRD) patterns of the as-fabricated CZY samples were recorded on a Bruker/AXS D8 Advance X-ray diffractometer operated at 40 kV and 200 mA using Cu Kα radiation and a Ni filter ($\lambda = 0.15406$ nm). Crystal phases were identified by referring the diffraction lines to those of the powder diffraction files−1998 ICDD PDF Database. Surface areas of the samples were measured via N_2 adsorption at −196 °C on an ASAP 2020 (Micromeritics) adsorption analyzer with the samples being outgassed at 250 °C for 2 h under a vacuum prior to measurements; surface areas were calculated according to the Brunauer−Emmett−Teller (BET) method. The scanning electron microscopic (SEM) images and energy-dispersive X-ray spectroscopic (EDXS) spectra of the samples were recorded by means of an apparatus (JEOL JSM 6500F or Gemini Zeiss Supra 55) operating at 10 or 20 kV. Before being transferred into the SEM chamber, the sample, ultrasound-dispersed in ethanol, was allowed to settle and dry on a holder before being introduced to a vacuum evaporator for gold deposition. By means of a JEOL-2010 instrument (operated at 200 kV), high-resolution transmission electron microscopy (HRTEM) images and selected area electron diffraction (SAED) patterns of the samples were obtained.

A thermogravimetric analysis (TGA) was conducted in a nitrogen flow of 100 mL min^{-1} at a ramp of 10 °C min^{-1} on an SDT Q600 instrument (TA). Fourier-transform infrared spectroscopic (FT-IR) spectra (500−5000 cm^{-1} with a resolution of 0.4 cm^{-1}) of the samples (1 wt % sample + 99 wt % KBr) were obtained on a Bruker Vertex 70 spectrometer. Laser Raman spectra of the CZY samples were obtained on a Raman spectrometer (Bruker RFS/100) equipped with a Nd:YAG laser (1064 nm) and an InGaAs detector; the laser power was 100 mW. The powdered samples were placed in a sample holder, and recording (from 200 to 800 cm^{-1} with a resolution of 4 cm^{-1}) was done in ambient atmosphere.

X-ray photoelectron spectroscopy (XPS; VG CLAM 4 MCD analyzer) was employed to determine the O 1s, Ce 3d, Zr 3d, Y 3d, and C 1s binding energies (BEs) of surface species of CZY samples with Mg Kα ($h\nu = 1253.6$ eV) as the excitation source. The instrumental resolution was 0.5 eV. Before XPS determination, the CZY samples were calcined in O_2 (flow rate, 20 mL min^{-1}) at 500 °C for 1 h for the removal of surface carbonate and adsorbed water. After being cooled to RT in the same atmosphere and purged in helium (flow rate, 40 mL min^{-1}), the samples were in turn transferred to the holder under the protection of helium in a transparent GLOVE BAG (Instruments for Research and Industry, USA), mounted to the spectrometer, outgassed in the preparation chamber (10^{-5} Torr) for 0.5 h, and introduced into the analysis chamber (3×10^{-9} Torr) for spectrum recording. The C 1s peak at 284.6 eV was taken as a reference for BE calibration.

Hydrogen temperature-programmed reduction (H_2-TPR) experiments were conducted with a sample (200 mg, 40−60 mesh) first pretreated *in situ* in O_2 (flow rate, 40 mL min^{-1}) at 500 °C for 1 h in a quartz fixed-bed U-shaped microreactor (i.d. = 9 mm). After cooling to RT in the same atmosphere, the CZY sample was exposed to a flow (50 mL min^{-1}) of 5% H_2 and 95% He (v/v) and heated at a rate of 10 °C min^{-1} from RT to 850 °C. The change in H_2 concentration of the outlet gases was monitored online on a chemical adsorption apparatus (Micromeritics Autochem II). The

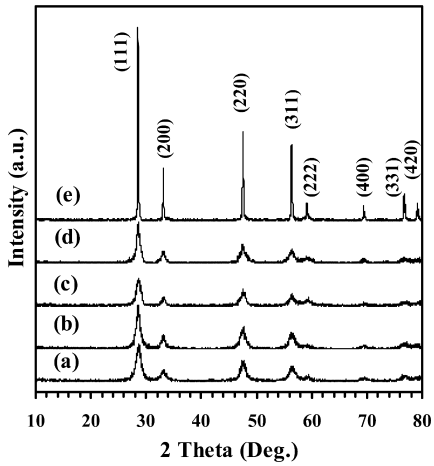

Figure 1. XRD patterns of (a) CZY-CTAB-120, (b) CZY-CTAB-160, (c) CZY-P123-100, (d) CZY-P123-120, and (e) CZY-P123-240.

signal peak was calibrated against that of the complete reduction of a known standard powder CuO (Aldrich, 99.995%).

3. Results and Discussion

3.1. Crystal Phase Compositions. Figure 1 shows the wide-angle XRD patterns of the CZY samples fabricated under different conditions. It is observed that the XRD patterns of the CZY samples were rather similar to those of cubic $Ce_{0.6}Zr_{0.4}O_2$ (JCPDS PDF# 38-1439) and can be well indexed, as indicated in Figure 1e. These XRD patterns also resemble those of cubic CeO_2,[16] $Ce_{0.6}Zr_{0.4}O_2$,[17] and $Ce_{0.7}Zr_{0.3}O_2$,[17b] reported by other researchers. Therefore, we can deduce that all of the samples were single-phase and of cubic fluorite-type crystal structure. The XRD lines of the CZY-P123-240 sample (Figure 1e), however, were much stronger in intensity than those of the CZY-CTAB-120 and CZY-CTAB-160 samples (Figure 1a,b) and those of the CZY-P123-100 and CZY-P123-120 samples (Figure 1c,d), implying that the former sample possessed a crystallinity much better than the latter four samples. Also, the latter four samples exhibited similar crystallinity due to the close intensity of their XRD lines (Figure 1a−d).

3.2. Morphologies and Crystal Types. The morphologies and crystal natures of the typical samples were investigated by means of SEM, HRTEM, and SAED techniques. Figure 2 shows the SEM and HRTEM images as well as the SAED patterns of the CZY-CTAB-120 and CZY-CTAB-160 samples. It is clearly observed that the two samples displayed a rodlike shape with different lengths (30 nm to 2 μm) and similar diameters (ca. 10 nm; Figure 2a,b,d,e); the sample obtained at a higher hydrothermal temperature also contained some irregular nanoparticles (Figure 2d). The recording of at least two light electron diffraction rings in the SAED patterns of the two samples reveals the formation of polycrystallites (Figure 2c,f); furthermore, the clearly observable lattice spacing was ca. 0.31 nm, coinciding with that (0.312485 nm) of the (111) plane of cubic CeO_2 (JCPDS PDF# 81-0792) or that (0.306400 nm) of the (111) plane of cubic $Ce_{0.6}Zr_{0.4}O_2$ (JCPDS PDF# 38-1439). Shown in Figure 3 are the SEM and HRTEM images, together with the SAED patterns, of the CZY-P123-100 sample. One can see that the CZY-P123-100 sample exhibited a spherical morphology with a diameter that ranged from 20 to 50 μm, and each CZY-P123-100 microsphere was composed of a large number of radially arrayed well-grown laminas, between which a weak interaction seems to exist due to the easy cracking of the microsphere, as observed in Figure 3a−e. The rough surface of each microsphere was formed by the external sides of laminas compiled in different directions (Figure 3e). From the SAED pattern (Figure 3f), one can realize that the CZY-P123-100 sample was polycrystalline. The well-defined lattice spacing was measured to be ca. 0.31 nm, corresponding to that of the (111) plane of the cubic-structured CZY crystal. With the rise in hydrothermal temperature from 100 to 120 °C, the as-fabricated CZY-P123-120 sample showed a shape of microbowknots. The bowknotlike CZY-P123-120 entities were constructed by a lot of nano- and microslices, with a width and length of 2−6 and 5−10 μm, respectively. These nano- and microslices were intimately aligned symmetrically along the reverse orientation of the center of the microbowknot, generating rather coarse surfaces of the ends of a microbowknot (Figure 4a−e). There was aggregation of the bowknotlike microentities. The lattice spacing of ca. 0.31 nm estimated from the HRTEM photograph (inset of Figure 4f) was quite close to those of the (111) plane of the above-mentioned cubic CeO_2 and $Ce_{0.6}Zr_{0.4}O_2$. The SAED pattern showed several diffraction rings, revealing the generation of a polycrystalline ceria−zirconia−yttria solid solution. With a further rise in the hydrothermal treatment temperature to 240 °C, the morphology of the as-obtained CZY-P123-240 sample changed significantly, and a micro-octahedral particle architecture can be observed clearly (Figure 5a−e). The dimensions of the high-temperature-derived CZY-P123-240 micro-octahedral particles were in the range of 100 nm to 2 μm. The HRTEM image of the CZY-P123-240 sample showed a clear lattice fringe direction attributed to the (111) plane, with its intraplanar spacing equal to 0.31 nm. The appearance of several bright diffraction rings in the SAED pattern (inset of Figure 5f) suggests the formation of polycrystallites.

It should be noted that the theoretical Ce/Zr/Y molar ratio of $Ce_{0.6}Zr_{0.3}Y_{0.1}O_2$ is 6:3:1. From the quantitative data obtained from the EDXS spectra (Figure S1 of Supporting Information), one can calculate the Ce/Zr/Y molar ratios of the above specifically shaped CZY samples, and they (5.85:3.04:1.00 for CZY-CTAB-120, 6.19:3.02:1.00 for CZY-P123-100, 5.92:2.83:1.00 for CZY-P123-120, and 6.02:2.98:1.00 for CZY-P123-240) were not far away from the theoretical Ce/Zr/Y molar ratio (6:3:1). Such a discrepancy might be due to the presence of experimental error in the EDXS measurements. Therefore, we believe that Zr^{4+} and Y^{3+} have been incorporated into the CeO_2 lattice.

The surface area was 100, 89, 70, and 30 m^2/g for the CZY samples with rodlike, spherical, bowknotlike, and

(16) Deshpande, A. S.; Pinna, N.; Smarsly, B.; Antonietti, M.; Niedererger, M. *Small* **2005**, *1*, 313.
(17) (a) Vidmar, P.; Fornasiero, P.; Kašpar, J.; Gubitosa, G.; Graziani, M. *J. Catal.* **1997**, *171*, 160. (b) Sugiura, M. *Catal. Surv. Asia* **2003**, *7*, 77.

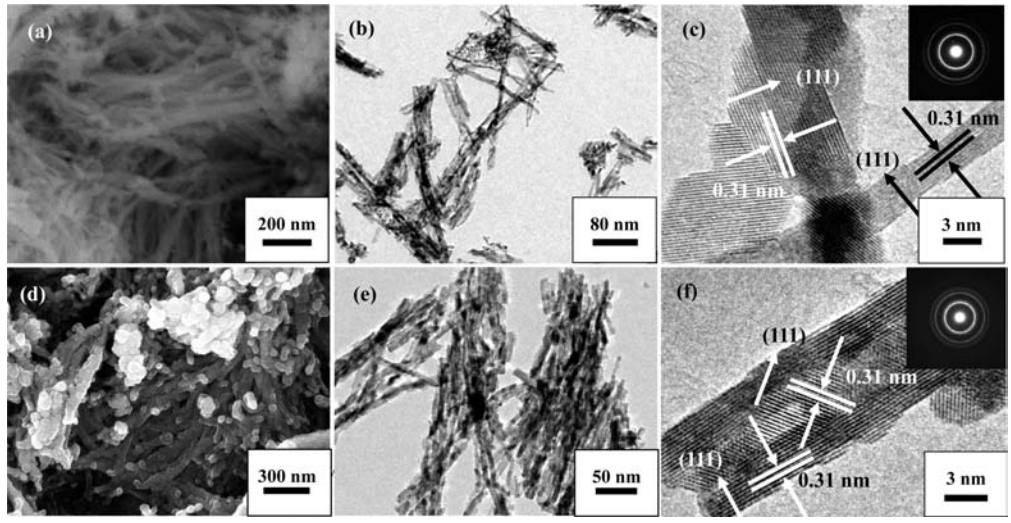

Figure 2. SEM (a,d) and HRTEM (b,c,e,f) images as well as their SAED patterns (insets) of (a−c) CZY-CTAB-120 and (d−f) CZY-CTAB-160.

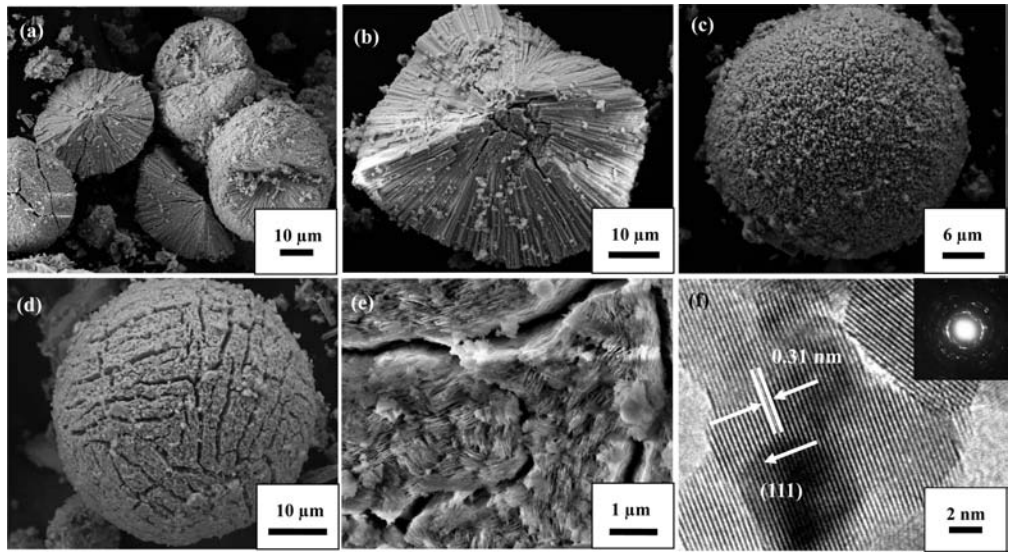

Figure 3. SEM (a−e) and HRTEM (f) images as well as the SAED pattern (inset) of CZY-P123-100.

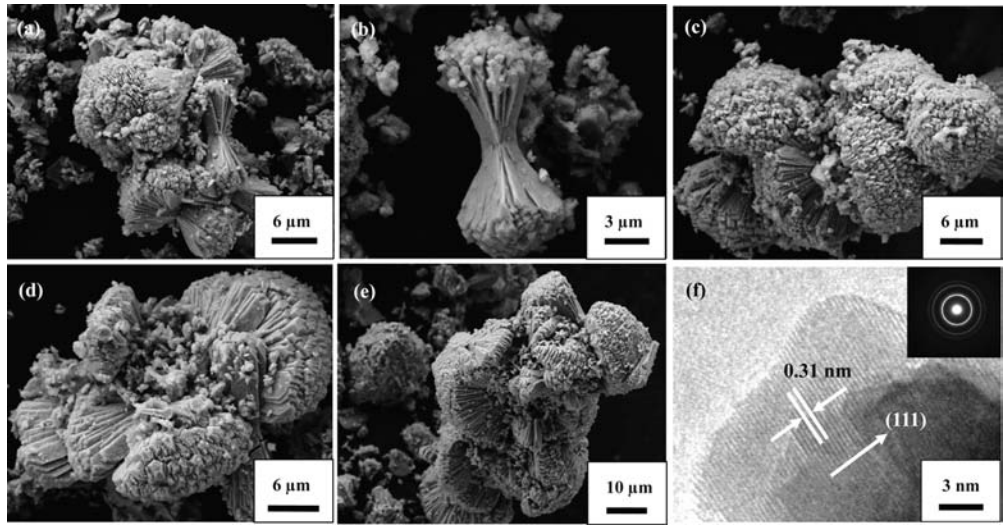

Figure 4. SEM (a−e) and HRTEM (f) images as well as the SAED pattern (inset) of CZY-P123-120.

octahedral shapes (Table 2), respectively. As can be seen from the N_2 adsorption−desorption isotherms of the CZY samples (Figure S2 of Supporting Information), the isotherms of the CZY-CTAB-120 and CZY-P123-240 samples displayed an almost linear middle section in the low-pressure portion (which is attributed to unrestricted monolayer-

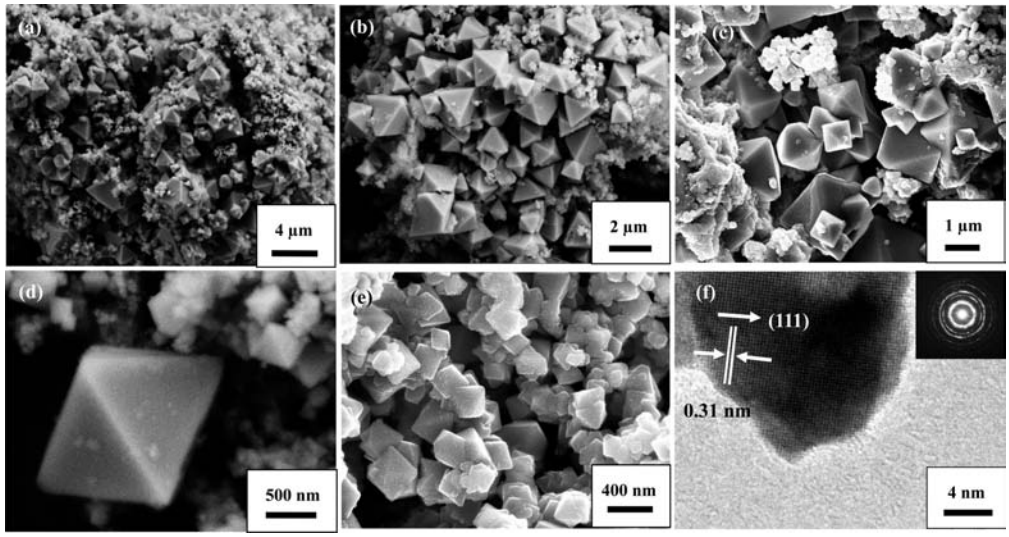

Figure 5. SEM (a−e) and HRTEM (f) images as well as the SAED pattern (inset) of CZY-P123-240.

Table 2. BET Surface Areas and Theoretical and Experimental H_2 Consumptions of the CZY Samples

sample	surface area (m^2/g)	theoretical H_2 consumption (mmol/mol_{Ce})[a]	experimental H_2 consumption (mmol/mol_{Ce})[b]
CZY-CTAB-120	100	403	293
CZY-P123-100	89	458	140
CZY-P123-120	70	420	203
CZY-P123-240	30	454	188

[a] The data were obtained according to the reduction of surface Ce^{4+} to Ce^{3+}. [b] The data were obtained from the quantification of the H_2-TPR reduction bands.

multilayer adsorption), suggesting that the two CZY samples were nonporous or were of intraparticle macropores.[18] The CZY-P123-100 and CZY-P123-120 samples exhibited a distorted type II isotherm associated with the existence of slit-shaped pores in materials,[19] which was substantiated by their nano/microslice-like structures (Figures 3 and 4). Although the size of the octahedrally shaped CZY-P123-240 particles was 1 order of magnitude smaller than that of the spherical CZY-P123-100 and bowknotlike CZY-P123-120 particles, their surface area was also smaller. This fact indicates the presence of "open" structures in the spherical and bowknotlike microentities, hence contributing to the higher surface areas.

3.3. Thermal Stability. In order to elucidate the weight loss processes, we did the XRD experiments of the CZY samples obtained after hydrothermal treatment and before calcination at 550 °C (called CZY precursors), and the results are shown in Figure 6A. It is observed that rather weak signals at $2\theta = 28.5°$, 33.1°, 47.5°, 56.3°, 59.1°, 69.4°, 76.7°, and 79.1° were detected in the XRD patterns of the CZY-P123-120 precursor (Figure 6A.c), demonstrating that only a small amount of crystalline $Ce_{0.6}Zr_{0.3}Y_{0.1}O_2$ solid solution was formed in the CZY-P123-120 precursor. However, the CZY-P123-240 precursor showed strong XRD peaks (Figure 6A.d) characteristic of a fluorite-type cubic crystal structure,

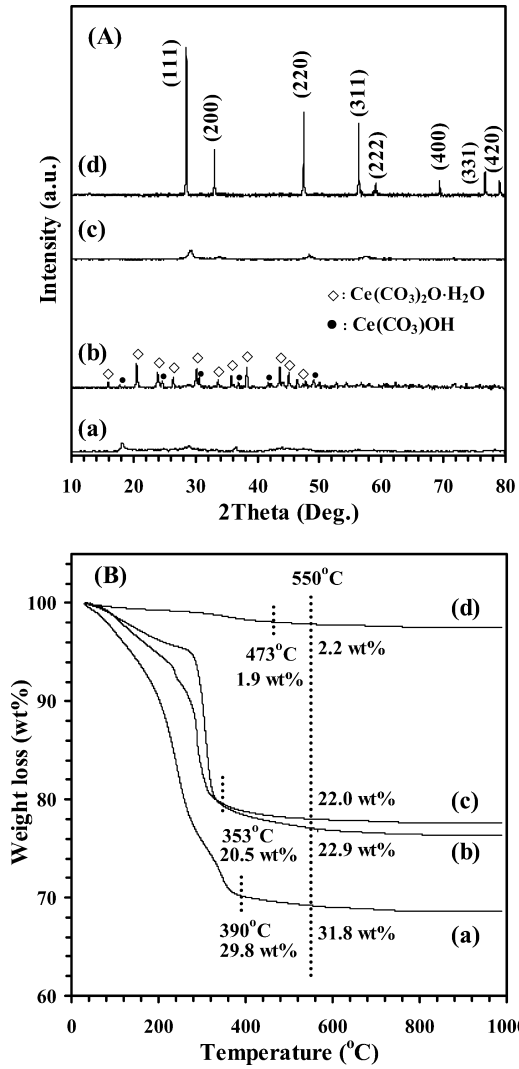

Figure 6. (A) XRD patterns and (B) TGA curves of (a) CZY-CTAB-120, (b) CZY-P123-100, (c) CZY-P123-120, and (d) CZY-P123-240 precursors.

demonstrating that under the high-temperature hydrothermal conditions a CZY solid solution was generated. After comparing the XRD patterns with the standard JCPDS files,

(18) Yan, H.; Blanford, C. F.; Holland, B. T.; Smyrl, W. H.; Stein, A. *Chem. Mater.* **2000**, *12*, 1134.
(19) Li, W.; Lu, A.; Weidenthaler, C.; Schüth, F. *Chem. Mater.* **2004**, *16*, 5676.

one can determine that the CZY-P123-100 precursor contained the orthorhombic $Ce(CO_3)_2O\cdot H_2O$ (JCPDS PDF# 44-0617) and hexagonal $Ce(CO_3)OH$ (JCPDS PDF# 52-0352) phases, together with a rather small amount of the CZY solid solution phase (Figure 6A.b). In the CZY-CTAB-120 precursor, there were very weak signals at $2\theta = 18.5°$, 29.1°, 36.6°, 44.9°, 48.0°, and 57.6° (Figure 6A.a), which were unidentified phase(s). Such an XRD pattern might be due to the formation of amorphous-like intermediates containing the Ce, Zr, and Y ions and the surfactant CTAB. To clarify this deduction, we measured the FT-IR spectra of the CZY precursors, and the results are shown in Figure S3 of the Supporting Information. It is clear that, in addition to the presence of adsorbed water and carbonate species in different coordination modes, there were residual surfactants (CTAB or P123) on or in the four CZY precursors, with their amounts being different from sample to sample. This result validates the formation of amorphous-like intermediates containing the metal elements and surfactants.

The TGA experiments for the CZY precursors were carried out to monitor the formation processes of CZY crystallites, and the results are shown in Figure 6B. There were two or three weight loss steps for the CZY-CTAB-120, CZY-P123-100, and CZY-P123-120 precursors (Figure 6B.a−c). The initial weight loss below 200 °C is due to the removal of adsorbed water, whereas that above 200 °C is due to decomposition of the $Ce(CO_3)_2O\cdot H_2O$ and $Ce(CO_3)OH$ phases and the amorphous-like intermediates formed via the interaction of metal sources and CTAB or P123, as well as due to generation of the CZY solid solutions, as confirmed by the XRD results of the CZY precursors (Figure 6A). From Figure 6B, one can see a weight loss of ca. 30 wt % (at 390 °C) for the CZY-CTAB-120 precursor and 21 wt % (at 353 °C) for the CZY-P123-100 and CZY-P123-120 precursors; at 550 °C, the weight loss was 31.8, 22.9, and 22.0 wt % for the above three CZY precursors, respectively, suggesting that most of the CZY solid solutions were formed during the calcination process. In the case of the CZY-P123-240 precursor, however, a rather low weight loss (below 550 °C) of 2.2 wt % (Figure 6B.d) was observed, demonstrating that a dominant amount of CZY solid solution was generated during the hydrothermal treatment process rather than during the calcination process, which was confirmed by the XRD result of the CZY-P123-240 precursor (Figure 6A.d). From Figure 6B, one can also find that no significant weight losses above 550 °C were observed. This indicates that calcining the CZY precursors at 550 °C could give rise to the single-phase CZY solid solution crystallites.

Figure 7 shows the FT-IR spectra of the CZY samples. It is observed that only two absorption bands at 1612 and 3430 cm^{-1} were detected on each CZY sample. Both absorption bands correspond to the stretching and bending vibrations of hydrogen-bonded surface OH groups of the physically adsorbed water.[20] There were no absorption bands at 3620 cm^{-1} (ascribable to the stretching vibration of bulk OH

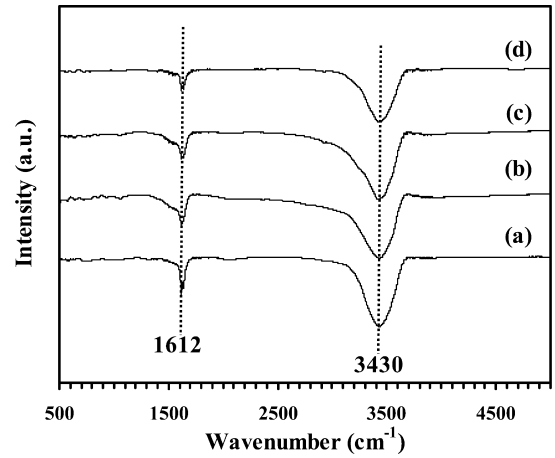

Figure 7. FT-IR spectra of (a) CZY-CTAB-120, (b) CZY-P123-100, (c) CZY-P123-120, and (d) CZY-P123-240.

groups[21]), at 1430 cm^{-1} (due to the symmetric stretching vibration of uni- or bi dentate carbonate[22]), at 870 cm^{-1} (assignable to the carbonate species[23]). In each CZY sample, no absorption bands were recorded at 2817 and 2914 cm^{-1}, assignable to the $-CH_2CH_2$ stretching vibrations, or at 1060 cm^{-1}, due to the C−O stretching vibration of the adopted surfactant molecules.[23a] It should be noted that several weak and broad absorptions due to the skeletal vibrations of the ceria−zirconia−yttria solid solutions[24] were observed in the wavenumber range of 500−800 cm^{-1} (Figure S4 of Supporting Information). The results indicate that (i) all of the $Ce(CO_3)_2O\cdot H_2O$, $Ce(CO_3)OH$, and amorphous-like intermediates formed via the interaction of metal sources and CTAB or P123 were totally decomposed to generate CZY solid solutions, (ii) no carbonates were retained in the CZY samples, and (iii) the residual surfactant amounts are rather low. These outcomes are confirmed by the results of XRD, XPS, and TGA investigations.

3.4. Crystal Structures. As a potential tool to obtain additional structural information, laser Raman is rather sensitive to the crystalline symmetry. Illustrated in Figure 8 are the laser Raman spectra of the CZY samples and their enlarged view. The Raman spectrum of each CZY sample showed a big band at ca. 461 cm^{-1} and weak bands at ca. 300 and 600 cm^{-1}. The big band corresponded to the triply degenerate F_{2g} mode and could be viewed as the symmetric O−Ce−O stretching mode.[25] It is well-known that only one Raman-active mode exists for the cubic fluorite-type structure of CeO_2.[26] The weak band at ca. 600 cm^{-1} corresponded to a doubly degenerate longitudinal optical mode of CeO_2,[27]

(20) Gadsden, J. A. *Infrared Spectra of Minerals and Related Inorganic Compounds*; Butterworths: London, U. K., 1975.

(21) Echterhoff, R.; Hoffmann, P.; Knözinger, E. *Proceedings of the 9th International Congress on Catalysis*, Calgary, Canada, 1988; Chemical Institute of Canada: Ottawa, ON, 2008; p 1418.
(22) Philipp, R.; Fujimoto, K. *J. Phys. Chem.* **1992**, *96*, 9035.
(23) (a) Thierry, B.; Zimmer, L.; McNiven, S.; Finnie, K.; Barbé, C.; Griesser, H. J. *Langmuir* **2008**, *24*, 8143. (b) Busca, G.; Lorenzelli, V. *Mater. Chem.* **1982**, *7*, 89.
(24) (a) Zaki, M. I.; Sheppard, N. *J. Catal.* **1983**, *80*, 114. (b) Mizuno, M.; Sasaki, Y.; Lee, S.; Katakura, H. *Langmuir* **2006**, *22*, 7137.
(25) Lin, X.-M.; Li, L.-P.; Li, G.-S.; Su, W.-H. *Mater. Chem. Phys.* **2001**, *69*, 236.
(26) Wachs, I. E.; Hardcastle, F. D.; Chan, S. S. *Spectroscopy* **1986**, *1*, 30.
(27) Spanier, J. E.; Robinson, R. D.; Zhang, F.; Chan, S.-W.; Herman, I. P. *Phys. Rev. B: Condens. Matter Mater. Phys.* **2001**, *64*, 245407.

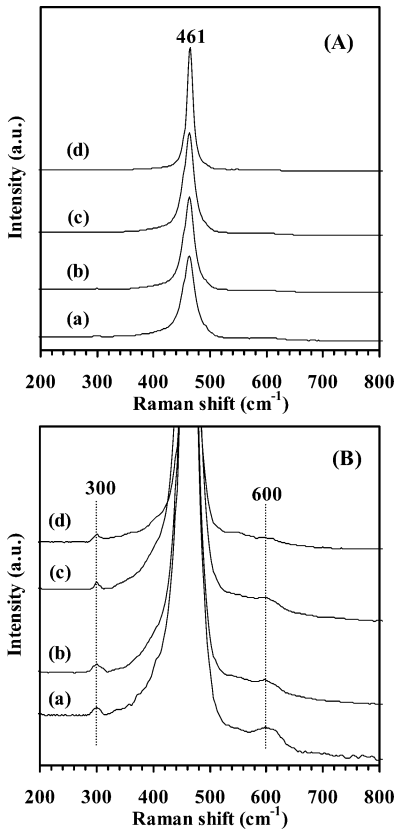

Figure 8. (A) Raman spectra of (a) CZY-CTAB-120, (b) CZY-P123-100, (c) CZY-P123-120, and (d) CZY-P123-240 and (B) their enlarged view.

and this band could be linked to oxygen vacancies in the CeO_2 lattice.[28] The weak band at ca. 300 cm^{-1} could be attributed to displacement of the oxygen atoms from their ideal fluorite lattice positions[29] or to the Ce−Zr−O stretching mode. The detection of these Raman bands for Ce−Zr−O, O−Ce−O, and Ce−Zr−Y−O stretching modes evidenced the presence of the same cubic phase as in the $Ce_{0.67}Zr_{0.33}O_2$ solid solution. One can also observe that the Raman band of the CZY-P123-240 sample (Figure 8A.d) was more symmetrical and sharper than those of the other three CZY samples (Figure 8A.a−c), indicating that the former sample possessed better crystallization than the latter three ones, which is in line with the XRD results (Figure 1). According to the literature, six Raman-active modes ($A_{1g} + 3E_g + 2B_{1g}$) are expected for the tetragonal zirconia (t-ZrO_2) phase,[30] but no Raman bands due to such a zirconia phase could be detected in the present investigation. These results provide a piece of supporting evidence that Zr^{4+} and Y^{3+} ions have been incorporated in the CeO_2 lattice. In other words, there is generation of single-phase $Ce_{0.6}Zr_{0.3}Y_{0.1}O_2$ solid solutions. It is noted that sintering of the CZY samples at high temperatures would give rise to the formation of oxygen vacancies, which perturbs the local metal−oxygen bond symmetry, leading to the relaxation of symmetry selection rules.[26]

3.5. Formation Mechanism. Although the exact formation mechanism of nanorod-like, microspherical, microbowknot-like, and micro-octahedral CZY particles is not clear, the results obtained in the present investigation indicate that the generation of nanorod-like, microspherical, microbowknot-like, and micro-octahedral CZY entities is likely to be due to the interaction of the initially formed nanostructured $Ce(OH)_4$, $Zr(OH)_4$, and $Y(OH)_3$ with the introduced surfactant (CTAB or P123) to generate CZY or amorphous-like intermediates containing Zr, Y (or Ce), and CTAB (or P123), as confirmed by the XRD results of the CZY precursors (Figure 6A.b−d). In the past years, a large number of studies have been focused on the effects of temperature, concentration, and surfactant composition on the structure (size, morphology, and aggregation number) of surfactant micelles. Among the above-listed parameters, temperature and surfactant composition have been found to be very crucial. With the rise in temperature, the morphology of the surfactant changes from spherical to cylindrical, rodlike, wormlike, or even lamellar-shaped.[31] Figure 9 illustrates the possible formation mechanism of nanorod-like, microspherical, microbowknot-like, and micro-octahedral CZY particles. Under hydrothermal conditions and in the presence of the surfactant, the primary Ce, Zr, and Y hydroxide nanoparticles formed due to the reaction of the metal nitrates and urea, which might assemble to form a number of rodlike nanoentities. On the one hand, these nanorod-like CZY precursors formed in the presence of CTAB further grow into CZY nanorods after calcination at 550 °C. On the other hand, the nanorod-like CZY precursors generated in the presence of P123 aggregate in an array of spherical, bowknotlike, or octahedral orientation, thus giving rise to the microspherical, microbowknot-like, or micro-octahedral CZY solid solution after thermal treatment at 550 °C. It has been accepted that the functional headgroups of the surfactant have coordination bonds or strong interactions with metal (Ce, Zr, Y) hydroxide nanoparticles and hence kinetically govern the growth rates of various faces of crystals, thus controlling the morphology.[32] It is reasonable to deduce that there is adsorption of the surfactant molecules on the well-aligned metal hydroxides via hydrogen bonding with the OH groups of Ce^{4+}, Zr^{4+}, and Y^{3+} or via loose coordination with these metal ions. Such an interaction between surfactant and metal hydroxides would be rather similar to that between P123 and $Mg(OH)_2$ in the synthesis of mesoporous MgO under the P123-aided hydrothermal conditions.[33] In addition, the primary $Ce(OH)_4$

(28) McBride, J. R.; Hass, K. C.; Poindexter, B. D.; Weber, W. H. *J. Appl. Phys.* **1994**, *76*, 2435.
(29) Reddy, B. M.; Khan, A.; Yamada, Y.; Kobayashi, T.; Loridant, S.; Volta, J. C. *J. Phys. Chem. B* **2003**, *107*, 11475.
(30) (a) Yashima, M.; Arashi, H.; Kakihana, M.; Yoshimura, M. *J. Am. Ceram. Soc.* **1994**, *7*, 1067. (b) Fernández López, E.; Sanchez Escribano, V.; Panizza, M.; Carnasciali, M. M.; Busca, G. *J. Mater. Chem.* **2001**, *11*, 1891.
(31) (a) Alexandridis, P.; Hatton, T. A. *Colloids Surf., A* **1995**, *96*, 1. (b) Hamley, I. Micellization in PEO-based block copolymers. In *Block Copolymers in Solution: Fundamentals and Applications*; John Wiley and Sons, Ltd.: Chichester, U. K., 2005. (c) Alexandridis, P.; Holzwarth, J. F.; Hatton, T. A. *Macromolecules* **1994**, *27*, 2414. (d) Nagarajan, R. *Colloids Surf., B* **1999**, *16*, 55. (e) Lehner, D.; Lindner, H.; Glatter, O. *Langmuir* **2000**, *16*, 1689.
(32) (a) Li, Z. Q.; Xiong, Y. J.; Xie, Y. *Inorg. Chem.* **2003**, *42*, 8105. (b) Huang, H. H.; Ni, X. P.; Loy, G. L.; Chew, C. H.; Tan, K. L.; Loh, F. C.; Deng, J. F.; Xu, G. Q. *Langmuir* **1996**, *12*, 909. (c) Sun, Y. G.; Xia, Y. N. *Adv. Mater.* **2002**, *14*, 833.
(33) Wang, G.; Zhang, L.; Dai, H.; Deng, J.; Liu, C.; He, H.; Au, C. T. *Inorg. Chem.* **2008**, *47*, 4015.

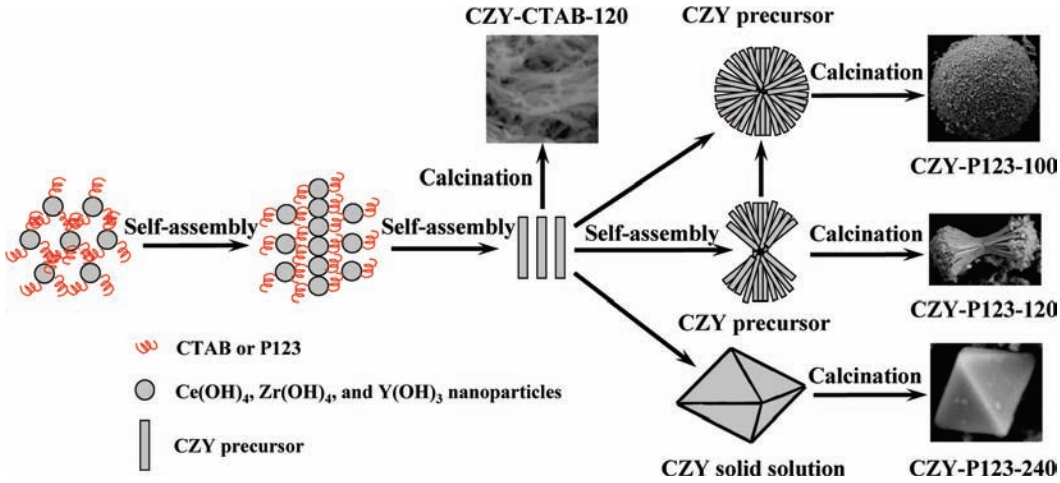

Figure 9. The schematic illustration of formation mechanisms of the CZY precursors and CZY solid solutions under surfactant-assisted hydrothermal and calcination conditions.

nanoparticles could also react with CO_2 released from the hydrolysis of urea to form $Ce(CO_3)_2O \cdot H_2O$ and $Ce(CO_3)OH$, as confirmed by the XRD result of the CZY-P123-100 precursor (Figure 6A.b). Therefore, the above formed metal- and surfactant-containing species could self-assemble layer by layer into the microspherical, microbowknot-like, or micro-octahedral CZY morphology. The nonionic polymer P123 has hydrophilic −O− and hydrophobic $-CH_2-CH_2-$ on the long chains. Water is a good solvent for P123, favoring the full extension of the polymer chains. The O atom of P123 can coordinate with metal ions. The more or less extended order of the polymer chain would provide an environment of organization for metal ions along the polymer backbone. The hydrothermal temperature also has an important effect on the interaction of the P123 polymer chain with the metal hydroxides, thus influencing the morphology of the product. At lower hydrothermal temperatures (100 and 120 °C), the CZY precursors display a microspherical and microbowknot-like architecture, respectively, in which the spherical microparticles were configured by a number of aggregated narrow nanorods or nanoplates, and such microspheres were easily broken from the center, as clearly seen from Figure 3a,b,d,e. With the rise in hydrothermal temperature from 100 to 120 °C, the as-fabricated microbowknot-like CZY entities were relatively robust, although they contained a smaller amount of aggregated narrow nanorods or nanoplates. When the hydrothermal temperature was raised to 240 °C, however, there was direct formation of octahedral CZY microparticles (rather than the CZY precursor) in the autoclave, as confirmed by the results of the TGA investigation (Figure 6B.d). It is an outcome due to the solid-state reaction of the metal hydroxides under high temperatures as well as high pressures within the autoclave. Therefore, the main morphologies of the CZY samples are governed by the hydrothermal temperature and nature of the surfactant. A similar conclusion has also been drawn by Buscaglia et al., who investigated the surfactant-assisted hydrothermal synthesis of β-$Ni(OH)_2$ with different morphologies (hexagonal platelets, hexagonal tabular mesocrystals, rosette- and flowerlike aggregates of lamellae, hexagonal prismatic mesocrystals, whiskers, spherical aggregates, spherical superstructures, and hollow spheres).[34] By adopting the hydrothermal method with various amino acids (L-lysine, L-glycine, L-glutamic acid, and L-aspartic acid) as crystallization modifiers and cerium oxalate as a Ce source, Zhang et al.[35] generated several hierarchical nanostructured ceria materials with dendritic microaggregates of rods, dumbbells, and spheres. These authors pointed out that the nature of the amino acid and the hydrothermal temperature played an important role in controlling the morphology of the ceria product.

3.6. Surface Oxygen Species, Surface Compositions, and Cerium Oxidation States. Figure 10 shows the O 1s, Ce 3d, Zr 3d, and Y 3d core-level XPS spectra of the CZY samples. It is seen from Figure 10A that there was an asymmetrical peak at BE = ca. 530 eV, which could be decomposed into two components at BE = 529.2 and 531.5 eV, attributable to the surface lattice oxygen (O_{latt}) and adsorbed oxygen (O_{ads}, e.g. O_2^-, O_2^{2-}, or O^-) species[14b,36] in or on the CZY samples, respectively. The presence of surface hydroxyl species could be left out because the samples were pretreated in an O_2 flow at 500 °C for 1 h, and the recording of their XPS spectra was carried out without exposure to the air. Another piece of supporting evidence is from their FT-IR results, in which no significant signals in the range of 3600−3750 cm^{-1} ascribable to the OH groups were detected in the CZY samples (Figure S5 of the Supporting Information). These oxygen species mainly originated from the CZY solid solutions. It has been reported that there was a presence of oxygen vacancies in $Ce_{1-x}Zr_xO_2$,[8b,37] and the doping of Y^{3+} to the lattice of ceria−zirconia solid solution could further increase the

(34) Buscaglia, M. T.; Buscaglia, V.; Bottino, C.; Viviani, M.; Fournier, R.; Sennour, M.; Presto, S.; Marazza, R.; Nanni, P. *Cryst. Growth Des.* **2008**, *8*, 3847.
(35) Zhang, G.; Shen, Z.; Liu, M.; Guo, C.; Sun, P.; Yuan, Z.; Li, B.; Ding, D.; Chen, T. *J. Phys. Chem. B* **2006**, *110*, 25782.
(36) (a) Galtayries, A.; Sporken, R.; Riga, J.; Blanchard, G.; Caudano, R. *J. Electron Spectrosc. Relat. Phenom.* **1998**, *88−91*, 951. (b) Zhu, L.; Yu, J. J.; Wang, X. Z. *J. Hazard. Mater.* **2007**, *140*, 205.
(37) (a) Balducci, G.; Kašpar, J.; Fornasiero, P.; Graziani, M.; Islam, M. S.; Gale, J. D. *J. Phys. Chem. B* **1997**, *101*, 1750. (b) Martínez-Arias, A.; Fernández-García, M.; Belver, C.; Conesa, J. C.; Soria, J. *Catal. Lett.* **2000**, *65*, 197.

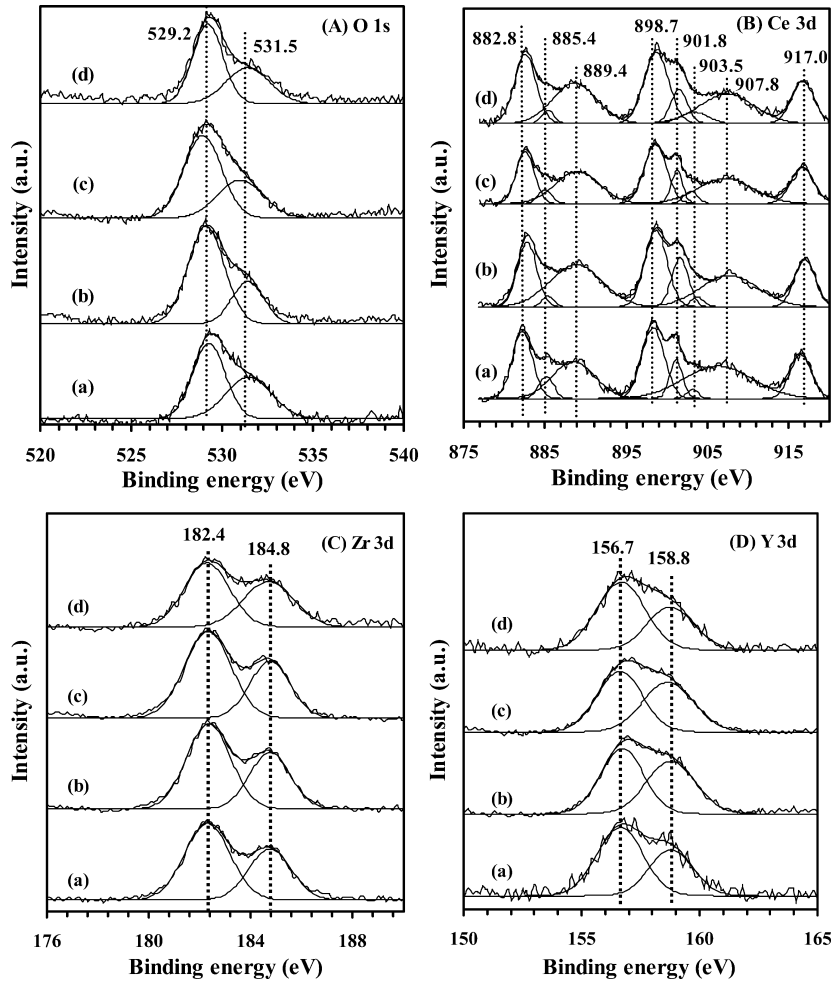

Figure 10. (A) O 1s, (B) Ce 3d, (C) Zr 3d, and (D) Y 3d XPS spectra of (a) CZY-CTAB-120, (b) CZY-P123-100, (c) CZY-P123-120, and (d) CZY-P123-240.

density of oxygen vacancies.[10a,14b] From Figure 10B, one can observe that there were two sets of signals: one was at BE = 882.8, 885.4, 889.4, and 898.7 eV, ascribable to the Ce $3d_{5/2}$, and the other was at BE = 901.8, 903.5, 907.8, and 917.0 eV, assignable to the Ce $3d_{3/2}$.[15a,38] The signals at BE = 885.4 and 903.5 eV were due to Ce^{3+}, whereas the ones at other BEs were due to Ce^{4+}.[15a,38] That is to say, the cerium in our CZY samples existed in tri- and tetravalency. Similar scenarios also occurred in the CeO_2,[39] $Ce_{1-x}Zr_xO_2$,[40] and $RE_{0.6}Zr_{0.3-x}Y_xO_2$[14] samples. From the Zr 3d XPS spectra of the four CZY samples (Figure 10C), one can observe two signals at BE = 182.4 and 184.8 eV, which could be assigned to Zr $3d_{5/2}$ and Zr $3d_{3/2}$, respectively.[41] In the Y 3d XPS spectra of each CZY sample (Figure 10D), there was an asymmetrical peak that could be decomposed to two components at BE = 156.7 and 158.8 eV, attributable to Y $3d_{5/2}$ and Y $3d_{3/2}$, respectively.[41] The results reveal that the Zr and Y ions in each sample were present in tetra- and trivalency, respectively. According to the XPS spectra, we calculated the surface compositions of the CZY samples, as shown in Table 1. It is observed that the surface Y/Ce atomic ratio of each sample was basically in agreement with its bulk atomic ratio, but there was a presence of Zr enrichment on the surface of each sample. For these CZY samples, the surface O_{ads}/O_{latt} and Ce^{3+}/Ce^{4+} atomic ratios increased in the same sequence of CZY-P123-100 < CZY-P123-240 < CZY-P123-120 < CZY-CTAB-120. On the basis of the principle of electroneutrality, we hence conclude that there was a presence of oxygen vacancies in the as-fabricated CZY samples. Usually, oxygen molecules are adsorbed at the sites of oxygen vacancies of anion-deficient materials. Therefore, it is reasonably expected that the oxygen adspecies should locate at the surface oxygen vacancies of CZY. The same order in surface O_{ads}/O_{latt} and Ce^{3+}/Ce^{4+} atomic ratios confirms that, in CZY, the higher the Ce^{3+} concentration, the more the oxygen adspecies amount is. It is well-known that $Ce_{1-x}Zr_xO_2$ materials have good oxygen storage and release abilities due to the presence of cerium ions with

(38) Wuilloud, E.; Delley, B.; Schneide, W. D.; Baer, Y. *Phys. Rev. Lett.* **1984**, *53*, 202.
(39) (a) Zhong, L. S.; Hu, J. S.; Cao, A. M.; Liu, Q.; Song, W. G.; Wan, L. J. *Chem. Mater.* **2007**, *19*, 1648. (b) Mai, H.-X.; Sun, L.-D.; Zhang, Y.-W.; Si, R.; Feng, W.; Zhang, H.-P.; Liu, H.-C.; Yan, C.-H. *J. Phys. Chem. B* **2005**, *109*, 24380. (c) Zhang, D.; Fu, H.; Shi, L.; Pan, C.; Li, Q.; Chu, Y.; Yu, W. *Inorg. Chem.* **2007**, *46*, 2446.
(40) (a) Vidal, H.; Kašpar, J.; Pijolat, M.; Colonb, G.; Bernal, S.; Cordón, A.; Perrichon, V.; Fally, F. *Appl. Catal., B* **2000**, *27*, 49. (b) Daturi, M.; Finocchio, E.; Binet, C.; Lavalley, J.-C.; Fally, F.; Perrichon, V.; Vidal, H.; Hickey, N.; Kaspar, J. *J. Phys. Chem. B* **2000**, *104*, 9186.
(41) Moulder, J. F.; Stickle, W. F.; Sobol, P. E.; Bomben, K. D. *Handbook of X-ray Photoelectron Spectroscopy*; Perkin-Elmer Co.: Waltham, MA, 1992.

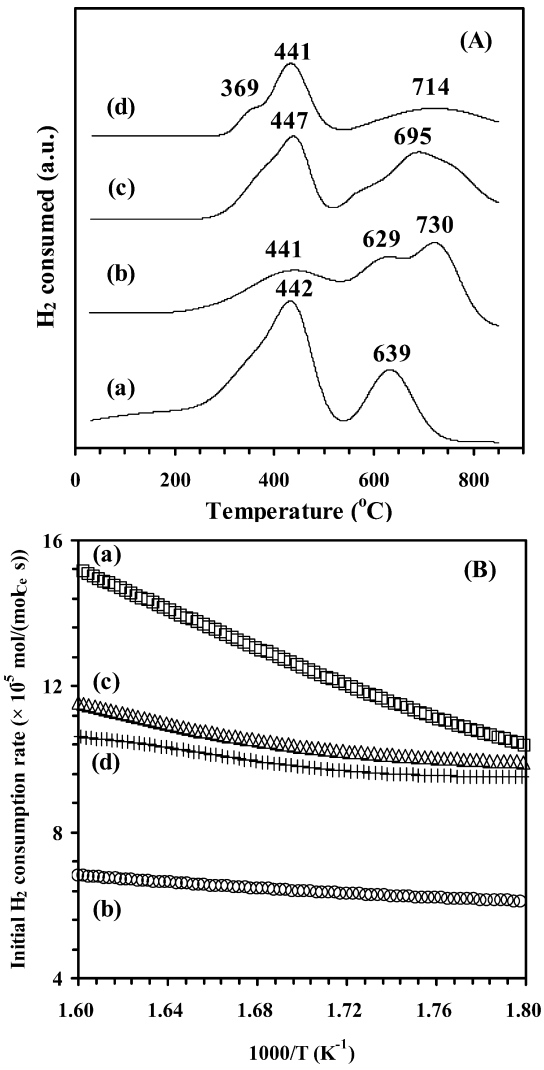

Figure 11. (A) H_2-TPR profiles and (B) H_2 consumption rates of (a) CZY-CTAB-120, (b) CZY-P123-100, (c) CZY-P123-120, and (d) CZY-P123-240.

mixed oxidation states,[39a,40a] which would facilitate the redox process of $Ce^{3+} \Leftrightarrow Ce^{4+}$.[14a,b]

3.7. Reducibility. Temperature-programmed reduction (TPR) is a convenient technique to evaluate the reducibility of solid oxide samples. Figure 11A illustrates the H_2-TPR profiles of the CZY samples. For each sample, there were two reduction processes: one at 240−550 °C and the other at 550−850 °C. The asymmetrical feature of either the low-temperature or high-temperature reduction bands implies the existence of at least two kinds of cerium species at various coordination environments. In addition to the similar low-temperature reduction profiles (with a shoulder at ca. 370 °C), one can observe a significant difference in the high-temperature reduction pattern among the four CZY samples. The reduction band at low temperatures could be attributed to the removal of surface oxygen adspecies and the reduction of surface Ce^{4+} to Ce^{3+},[3c,42] and the H_2 consumption was 293, 140, 203, and 188 mmol mol_{Ce}^{-1} for the nanorod-like, microspherical, microbowknot-like, and micro-octahedral CZY samples, respectively. The reduction band at high temperatures could be ascribed to the reduction of bulk Ce^{4+} to Ce^{3+},[3c,42] and the corresponding H_2 consumption was 156, 218, 255, and 131 mmol mol_{Ce}^{-1}. Apparently, the reducibility at lower temperatures (240−550 °C) increased in the order microspherical CZY-P123-100 < micro-octahedral CZY-P123-240 < microbowknot-like CZY-P123-120 < nanorod-like CZY-CTAB-120, whereas the total H_2 consumption followed a sequence of micro-octahedral CZY-P123-240 < microspherical CZY-P123-100 < nanorod-like CZY-CTAB-120 < microbowknot-like CZY-P123-120. Assuming that all of the cerium ions were in tetravalency and reduced to Ce^{3+}, one can obtain the H_2 consumption of 500 mmol mol_{Ce}^{-1} for the CZY samples. If the Ce^{3+}/Ce^{4+} molar ratios on the surface were the same as those in the bulk of the CZY samples, the theoretical H_2 consumptions of the CZY samples can be estimated (Table 2). Obviously, the experimental value was lower than the theoretical one for the same sample. It means that (i) only part of the Ce^{4+} ions could be reduced to Ce^{3+} ions below 550 °C, and (ii) the Ce^{3+}/Ce^{4+} molar ratio on the surface was different from that in the bulk of each CZY sample (with the nanorod-like CZY-CTAB-120 sample being the exception).

In order to better evaluate the reducibility of the CZY samples, we adopted the initial H_2 consumption rate in the reduction temperature range of 282−352 °C (corresponding to less than 25% H_2 consumption of the first reduction band), where no phase transformation took place, and the results are shown in Figure 11B. It is clear that (i) the nanorod-like CZY-CTAB-120 sample exhibited a much higher initial H_2 consumption rate than the microspherical CZY-P123-100 sample, and (ii) the microbowknot-like CZY-P123-120 was slightly higher than the micro-octahedral CZY-P123-240 sample in initial H_2 consumption rate. Also, the initial H_2 consumption rates of both samples were between those of the nanorod-like and microspherical CZY samples. Such a sequence of initial H_2 consumption rate is in good agreement with the H_2 consumption at low temperatures of the CZY samples. These results suggest that there is a presence of morphology-dependent reducibility for the CZY samples. Other authors also reported a similar morphological effect on the reduction behaviors of CeO_2.[5b,15a,35,43] For example, Yang et al. observed that the H_2 consumption of cubelike ceria nanoparticles was 4−5 times higher than that of the conventional irregular CeO_2 material, and they attributed the enhancement in reducibility to the peculiar particle morphol-

(42) (a) Jacobs, G.; Graham, U. M.; Chenu, E.; Patterson, P. M.; Dozier, A.; Davis, B. H. *J. Catal.* **2005**, *229*, 499. (b) Di Monte, R.; Fornasiero, P.; Graziani, M.; Kašpar, J. *J. Alloys Compd.* **1998**, *275−277*, 877. (c) Markaryan, G. L.; Ikryannikova, L. N.; Muravieva, G. P.; Turakulova, A. O.; Kostyuk, B. G.; Lunina, E. V.; Lunin, V. V.; Zhilinskaya, E.; Aboukaï¨s, A. *Colloids Surf. A* **1999**, *151*, 435. (d) Kulyova, S. P.; Lunina, E. V.; Lunin, V. V.; Kostyuk, B. G.; Muravyova, G. P.; Kharlanov, A. N.; Zhilinskaya, E. A.; Aboukaï¨s, A. *Chem. Mater.* **2001**, *13*, 1491. (e) Masui, T.; Peng, Y.; Machida, K.-I.; Adachi, G.-Y. *Chem. Mater.* **1998**, *10*, 4005. (f) Ozaki, T.; Masui, T.; Machida, K.-I.; Adachi, G.-Y.; Sakata, T.; Mori, H. *Chem. Mater.* **2000**, *12*, 643.

(43) (a) Yang, Z.; Zhou, K.; Liu, X.; Tian, Q.; Lu, D.; Yang, S. *Nanotechnology* **2007**, *18*, 185606. (b) Zhou, K.; Yang, Z.; Yang, S. *Chem. Mater.* **2007**, *19*, 1215. (c) Liotta, L. F.; Pantaleo, G.; Maculuso, A.; Marcì, G.; Gialanella, S.; Deganello, G. *J. Sol-Gel Sci. Technol.* **2003**, *28*, 119.

ogy of ceria.[43a] After working on the synthesis and catalytic properties of spindlelike, rodlike, and spherical ceria for CO oxidation, Yu and co-workers pointed out that the different morphologies gave rise to various oxygen vacancies and Ce^{4+} reduction extents of CeO_2, thus directly influencing their catalytic performance for the addressed reaction.[15a] As shown in Table 2, the experimental H_2 consumptions of the nanorod-like, microbowknot-like, and micro-octahedral CZY samples (188−293 mmol mol_{Ce}^{-1}) are much higher than that of the CeO_2 nanotubes (130 mmol mol_{Ce}^{-1}) reported by Zhou et al.,[43b] and also significantly higher than that of CeO_2 nanoparticles (19 mmol mol_{Ce}^{-1}).[5b] Although the experimental H_2 consumptions of our CZY samples (140−293 mmol mol_{Ce}^{-1}) are lower than those of the CeO_2-ZrO_2 samples with different Ce/Zr atomic ratios (220−448 mmol mol_{Ce}^{-1}) reported by Narula et al.,[10b] the temperatures of the first reduction band of the former samples (below 450 °C) are much lower than those of the latter samples (above 600 °C). On the basis of the above considerations, we conclude that the morphology of CZY has an important effect on its low-temperature reducibility.

4. Conclusion

In summary, fluorite-type cubic $Ce_{0.6}Zr_{0.3}Y_{0.1}O_2$ polycrystalline solid solutions with nanorod-like, microspherical, microbowknot-like, and micro-octahedral shapes have respectively been fabricated hydrothermally with CTAB at 120 °C for 72 h and with P123 at 100, 120, and 240 °C for 48 h, followed by calcination in an air flow at 550 °C for 3 h. The nature of the surfactant and the temperature of hydrothermal treatment have a great influence on the morphology of CZY particles. The formation mechanism could be explained reasonably. The copresence of Ce^{3+} and Ce^{4+} in CZY samples gives rise to the generation of oxygen vacancies. There is a good relationship between low-temperature reducibility and morphology of the CZY samples, with their reducibility at low temperatures (240−550 °C) increasing according to the order of micro-octahedral CZY < microspherical CZY < microbowknotlike CZY < nanorodlike CZY. It is concluded that the CZY solid solutions exhibited strong morphology-dependent low-temperature reducibility.

Acknowledgment. We gratefully acknowledge the financial aid from the NSF of China (Grant No. 20473006), the PHR200907105 of the Beijing Municipal Commission of Education, the PHR (IHLB) of Beijing Municipality, and the Project (Grant Nos. Guo-Ren-Bu-Fa [2004] 99 and Jing-Ren-Fa [2004] 111).

Supporting Information Available: EDXS spectra, N_2 adsorption−desorption isotherms, and FT-IR spectra from 500−800 cm^{-1} and 3600−4000 cm^{-1} of the as-fabricated CZY samples and FT-IR spectra of the CZY samples obtained after hydrothermal treatment and before calcination. This information is available free of charge via the Internet at http://pubs.acs.org.

IC802195J